Improving the Rate Capability of $LiFePO_4$ Electrode by Controlling Particle Size Distribution

Yin Zhang,[1,2,3] Jose A. Alarco,[1,z] Jawahar Y. Nerkar,[1] Adam S. Best,[2,*] Graeme A. Snook,[4,*] and Peter C. Talbot[1]

[1]Institute for Future Environments and Science and Engineering Faculty, Queensland University of Technology (QUT), Brisbane QLD 4001, Australia

[2]CSIRO Manufacturing, Clayton South, Victoria 3169, Australia

[3]CRRC Qingdao Sifang Rolling Stock Research Institute Co., Ltd., Qingdao 266031, China

[4]CSIRO Mineral Resources, Clayton South, Victoria 3169, Australia

*Electrochemical Society Member.

[z]E-mail: jose.alarco@qut.edu.au

Abstract

In this study, the rate performance of a $LiFePO_4$ (LFP) electrode has been enhanced by optimization of the particle size distribution of the LFP particles. Two LFP samples with different particle sizes (~50 and ~ 350 nm) are mixed with various ratios and the electrochemical performance has been evaluated. Reduction of the contact resistance and increase of the Li diffusion coefficient have been achieved. The electrode with a mixing ratio of 50:50 shows an improved initial capacity at C/10 and superior rate capability compared with the two pristine materials.

Introduction

As one of the commercial cathode materials for rechargeable Li-ion batteries (LIBs), $LiFePO_4$ (LFP) offers many merits compared with conventional cathodes, such as environmental friendliness, low cost, good safety, good cycling ability and a flat charge-discharge voltage plateau at relatively high potential of ~3.45 V versus Li/Li^+. Although LFP has had a wide-spread application in commercial LIBs in the last two decades[1, 2], its application in the high-power scenario has been

somewhat limited by its poor intrinsic electronic (~10^{-9} S/cm) and ionic conductivities (10^{-13} to 10^{-16} cm^2/s) [3]. Hence, considerable efforts have been made to improve its rate capability. Olivine-type LFP has an orthorhombic lattice structure with space group Pnma [4]. The oxygen ions form strong covalent bonds with phosphorus ions to form PO_4^{3-} , which can stabilize the three-dimensional frame work and provide safety and excellent cyclic performance[5]. However, the strong covalent oxygen bonds also lead to low ionic diffusivity and poor electronic conductivity[6]. Therefore, modifications of LFP to improve the conductivity have drawn much attention. It has been reported that by keeping the particles at nanoscale size, the rate performance of LFP can be significantly improved[7-9]. Kim et al.[9] achieved LFP nano-particles with a reversible capacity of 166 mAh/g and an excellent rate capability of 50 mAh/g at 60C, while Bauer et al.[8] achieved 14, 000 W/kg with 28 % of the theoretical capacity preserved.

In order to understand the surprising improvement in kinetics of the intrinsically insulating LFP material, the charge transport mechanism and phase diagram of $Li_{1-x}FePO_4$ ($0<x<1$) have been extensively investigated. Due to the lack of continuous LiO_6 octahedra in the direction of the a-axis and c-axis, lithium ions in the lattice of LFP can only migrate along the b-axis[10, 11]. This one-dimensional diffusion channel, which is easily blocked by crystal defects, has been blamed for the low Li diffusion rate. Therefore, the ionic conductivity of LFP can be enhanced by minimizing the particle size, as the reduced dimensions of nano particles shorten the diffusion path of Li ions. Besides, the Li migration through the channels in nano particles is easier than in micro particles, because nano particles exhibit lower density of lattice defects[12]. It has been found that the solubility limit of Li in the LFP structure is highly dependent on the particle size, where nano particles have higher solubility limit than micro particles[13-15]. The shrinking of the miscibility gap has a strong influence on the phase transition of LFP during charging and discharging. The result of Meethong et al.[16] suggested that the miscibility gap would completely disappear when the particle size was below 15 nm at room temperature. It is believed that the shrinking of the miscibility gap is responsible for the improvement of the rate performance of LFP. In the meantime, the fracture caused by the lattice mismatch of the two phases has been reported to be eliminated in nano LFP particles[17], resulting in better cycling performance. By electrochemical impedance spectroscopy (EIS) and in-situ X-ray diffraction

technology (XRD), the particle-by-particle[18-20] and hybrid (single-particle) phase-transition[20, 21] models have been confirmed for nano and micro LFP particles, respectively. In addition, a phase transition ahead of the charging and discharging processed of nano LFP has been recently reported[22], which is related to the weaker memory effect compared with micro LFP .

On the other hand, minimizing particle size can also bring problems. The tap density of nano-sized particles is generally lower than that of micro-sized particles, which would decrease the energy density of the cell. The nano-sized particles tending to agglomerate make the homogeneous dispersion of the conductive carbon during electrode fabrication very difficult[23]. It should be noted that when the particle sizes are below 100 nm, the fraction of the material at the particle surface increases adruptly[14], leading to lower stability due to the increased surface energy. More severe self-discharge has been found in nano LFP of ~ 25 nm compared with micro LFP of ~ 2 μm[24]. Moreover, impurity phases are reportedly easier to form during carbon coating on the surface of nano LFP[25], whose influence on electrochemical properties is ambiguous in the literature[26-29]. The manufacturing cost also increases with the reduction of particle size without sacrificing phase purity. After weighing the pros and cons, an optimum particle size for high-power applications has been suggested to be in the range of 200–400 nm[30].

In this research, a new method to improve the rate performance LFP electrode has been proposed. By making a mix of different particle sizes (ratio of nano and micro particles) of LFP with different Li insertion/extraction mechanism in the electrode, the charge transfer resistance can be significantly reduced leading to an enhancement of high-power capability. The electrochemical performance of the optimized electrode has been carefully evaluated. The kinetics of the mixed electrode has been discussed in detail.

Experimental

Synthesis

The LFP samples with two different particle sizes were synthesized using a solution-based method. Oxalic acid dihydrate (≥99%, Sigma-Aldrich) and Fe oxalate dihydrate (99%, Sigma-Aldrich) were mixed in deionized water first. The molar ratios of oxalic acid and Fe oxalate are 1.5:1 and 0.85:1 for

the nano- and micro-sized samples, respectively. 30 wt. % H_2O_2 was slowly added into the mixture under magnetic stirring to dissolve Fe oxalate in accordance with the following reaction,

$$2FeC_2O_4 \cdot 2H_2O + C_2H_2O_4 \cdot 2H_2O + 2H_2O_2 \rightarrow Fe_2(C_2O_4)_3 + 8H_2O + O_2$$

The temperature was controlled below 65 °C during this process to avoid the formation of impurities. Stoichiometric amounts of Li_2CO_3 (≥ 99%, Sigma-Aldrich) and H_3PO_4 (85 wt. %) were added into the solution. A small excess of Li (3 molar %) from the stoichiometric amount, was added to the solution, which, from our experience, leads to more reproducible, improved performance. 1% (based on the weight of final product) of polyethylene glycol (PEG) was added to obtain nano particles. The resultant clear green solution was drawn into a reactor and reacted at 300 °C for 1 hour under vacuum. The resultant precursors were ring milled and calcined at 550 °C and 710 °C for 1 hour under Ar atmosphere to form the nano and micro $LiFePO_4$ particles. The obtained powders were mixed with 8 wt. % sucrose and calcined at 710 °C for 1 hour with Ar atmosphere for carbon coating.

Characterization

The structure and morphology of the powder samples were characterized by X-ray diffraction (XRD), scanning electron microscopy (SEM) and transmission electron microscopy (TEM). XRD was collected on a PANalytical X'Pert pro diffractometer with Co-K_α radiation, over a 2θ range between 15˚ and 90˚ with a 2θ step size of 0.017. The Rietveld refinement was conducted using HighscorePlus v4.8 software. The morphology and microstructure of the samples were investigated with a JEOL 7001 SEM and JEOL 2100 TEM. The microstructure of the coated electrodes was also characterized using SEM on polished cross-section embedded in resin. The oxidation states on the surface of the samples was investigated with X-ray photoelectron spectroscopy (XPS, Kratos AXIS Supra photoelectron spectrometer) using a focused monochromated Al K_α radiation (hν = 1486.6 eV). The spectra were calibrated using the C 1s peak at 285.0 eV. Carbon analyses were conducted using a LECO TruMac CNS analyser. The furnace temperature for the sample was 1300 °C. Inductively coupled plasma (ICP) was used to analyse the elemental compositions. 0.2g of each sample was digested in 4 mL of a solution of 20 wt.% of HCl and 20 wt.% of HNO_3 in deionized water. Solid residues were filtered out and attributed to or associated with undissolved carbon contents.

Particle surface characteristics were also examined with Raman spectroscopy with a Renishaw inVia Microscope equipped with a long working distance 50× objective lens and a 534 nm Ar+ laser light source. The power was controlled at 1mW to avoid damaging the sample during measurement. The near-edge X-ray absorption fine structure (NEXAFS) were obtained using soft X-ray absorption spectroscopy (sXAS) at the soft X-ray beamline of Australian Synchrotron (AS). The NEXAFS spectra were simultaneously collected in total electron yield (TEY), partial electron yield (PEY) and total fluorescence yield (TFY) modes with a step size of 0.1 eV. All the spectra were normalized to I_0, which is a signal proportional to the X-ray flux hitting the sample obtained with a gold mesh with about 90 % transmission, to get a flux independent measurement.

Electrochemical testing

The electrochemical properties of the pristine materials and the blended samples were evaluated by constructing 2032 half cells. The slurry was prepared by mixing 90% active material powder, 5% Super P, 5% PVDF (Arkema Kynar® HSV 900 homopolymer) and NMP solvent (99.5%, Sigma-Aldrich). The slurry was cast on carbon coated Al foil with the loading of ~5 mg/cm^2. The 2032 coin cells were assembled inside a glovebox with lithium foil as anode and 1 M $LiPF_6$ EC: DEC (1:1 by vol., Novolyte, BASF) electrolyte. Galvanostatic and cyclic voltammetry testing were carried out utilizing a battery test system (BioLogic, VMP-300) at room temperature. Electrochemical impedance spectroscopy (EIS) was conducted with a sine wave signal in the frequency range from 1MHz to 1 mHz and amplitude of 1 mV.

Results and discussion

Material characterization

The XRD patterns and the Rietveld refinements of the synthesized LFP samples are shown in Figure 1. The patterns are entirely indexed as olivine $LiFePO_4$ (ICDD: 98-016-2282) with the space group Pnma, which confirms the phase purity of the LFP samples. The crystallite sizes calculated with the Sherrer equation are 65.0 nm and 42.3 nm for LFP samples calcined at 710 and 550 °C respectively. The Rietveld refinement results are summarized in Table 1. As the existence of anti-site defect TM_{Li} (transition metal ions occupy Li site) has been reported present in olivine phosphates [3-9],

the Li site has been left partially occupied with Fe ions while carrying out the refinement. The lattice parameters of the as-prepared samples are in good agreement with previous studies[31], while the sample sintered at 710 °C exhibits slightly larger cell volume than that sintered at 550 °C. The sample sintered at 710 °C has lower level of anti-site defects suggesting a better crystallinity resulted from the higher temperature calcination. The granular morphologies of the samples are illustrated in Figure 2. Both samples have the granular morphology. The average particle sizes are ~350 and ~50 nm for samples calcinated at 710 and 550 °C respectively, indicating polycrystalline for the sample sintered at 710 °C. Both as-prepared LFP samples are well crystallized with a coating layer of carbon (Figure 2b and d). The as-prepared samples are labelled as LFP-350 and LFP-50 according to their particle sizes respectively. The mole ratios of Li:Fe:P of the samples obtained with ICP are shown in Table 2. The ratio is typically within ±4% of the expected 1:1:1[32]. Both of the as prepared samples show the slight Li excess, deliberately introduced. As summarized in Table 2, about 2.8% of carbon has been determined for LFP-50, which is higher than the value for LFP-350 (about 1.9 %). As the LFP-50 has much larger surface area than LFP-350, about 49 ($=7^2$) times, estimated by approximating the particles to spheres, a much thinner average carbon coating may be expected.

High-resolution XPS has been carried out to investigate the surface state of the samples. As shown in the Fe-2p spectra in Figure 2c and f, the Fe ions on the surface exhibit mixed valence states for both samples. Although the samples have slight Li excess, no peaks of impurity phases are detected in the XRD patterns. The ratio of Fe^{2+} and Fe^{3+} calculated from the peak area are about 50:50 (as summarized in Table 3), even though carbon is supposed to provide a protection layer to avoid oxidation. The presence of Fe^{3+} suggests the presence of a Li-depletion layer around the particle in order to keep electrical neutrality. Similar Li-depletion layer has also been observed in carefully-prepared LFP [29], even when crystallized with hydrothermal in the presence of 3 times excess Li. The excess Li of the as prepared samples may result in other defects preferably in the bulk, e.g. Li antisites (Li on Fe sites), which is found to have low formation energy[33].

The as-prepared samples are further investigated using synchrotron-based sXAS. NEXAFS spectra are illustrated in Figure 3. All the displayed spectra have been normalized to peak maxima for

comparison. The Fe L-edge spectra with TEY mode are illustrated in Figure 3a. The Fe L-edge is considered stemming from the dipole-allowed Fe-2p to Fe-3d transition, which probes the unoccupied states of Fe-3d character. Therefore, the changes in the peak shapes and energy positions can give an indication of the oxidation state of the surface Fe. The Fe L-edge displays two groups of peaks, labelled L_3 and L_2, due to the core-hole spin-orbit-coupling splitting of the $2p_{1/2}$ and $2p_{3/2}$ orbitals. As the two main peaks located at 707.3 and 709.2 eV for Fe^{2+} and Fe^{3+} have different relative intensity[34-36], the change of the intensity ratio of these two peaks (I_{707}/I_{709}) can be associated to the oxidation state change of surface Fe ions. According to Figure 3a, LFP-50 displays lower I_{707}/I_{709} compared with LFP-350, suggesting more existence of Fe^{3+} on LFP-50 particle surface. O K-edges of the as-prepared sample are illustrated in Figure 3b and c. The O K-edge originates from the O-1s to O-2p transition, while the pre-edge located at 531.7 eV is attributed to O-2p weighting of states with predominantly Fe-3d character[37, 38] and the main absorption is attributed to oxygen p character hybridized with Fe 4s and 4p states[39, 40]. Since the pre-edge peak has been reported to be sensitive to the Li ion (de)intercalation[41, 42], the relatively higher pre-edge intensity provides additional evidence for higher level of surface Fe oxidation for LFP-50. By acquiring EY (TEY and PEY) and TFY signals simultaneously, the information on the surface and bulk can be obtained at the same time, as the fluorescent X-rays and Auger electrons have different escape depths (~3000 Å for fluorescent X-rays and ~50Å for Auger electrons) [41]. More surface information can be obtained with the PEY mode because it is more surface-sensitive compared with the TEY mode[43]. Therefore, the relatively higher pre-edge intensity in EY modes provides more evidence of surface Li depletion, which is in good agreement with the XPS results and earlier investigations[44-46].

Electrochemical performance of pristine materials

The electrochemical performance of the pristine LFP samples are evaluated first. The charge and discharge behaviours of the two samples are illustrated in Figure 4. Both samples exhibit voltage plateaus at ~3.45 V at C/10 (1C=170mA/g), suggesting the phase transition of $LiFePO_4$ and $FePO_4$ during charge and discharge. LFP-50 shows a slightly higher capacity (150 mAh/g) and lower polarization (~49 mV) at C/10 compared with LFP-350 (146 mAh/g and ~ 64 mV). However, LFP-50 starts to lose the initial flat voltage plateau and shows a sloping voltage profile with the increase of the

applied current when the C-rate goes beyond C/5 (as shown in Figure 4c). Although a better rate performance is generally expected for the samples with smaller particle size, LFP-350 exhibits a higher capacity when the C-rate is higher than 1C in this study (as shown in Figure 4a). Moreover, a voltage overshoot has been noticed in the LFP-350 electrode at the beginning of the charge and discharge in the whole measured C-rate range in this study, and it gets more pronounced with increasing C-rate, while no similar feature is observed for the LFP-50 samples.

Electrochemical performance of mixed LFP electrodes

The Galvanostatic charge-discharge profiles of the pristine and mixed LFP electrodes at C/10 are illustrated in Figure 5a. The mixed electrodes are labelled with the ratio of LFP-50 and LFP-350. The mixed electrodes exhibit voltage plateaus in between those of LFP-50 and LFP-350 during charging, and higher than those of both pristine electrodes during discharging. Among these, the electrode with a mix ratio of 50:50 shows the smallest polarization. Furthermore, the voltage overshoot for LFP-350 has been erased with the addition of LFP-50 particles. Most of the mixed electrodes show capacities between LFP-50 and LFP-350, while the electrode of 50:50 exhibits a specific capacity boost (~162 mAh/g).

A comparison of the rate capability has been conducted. The voltage profiles at various C-rates are displayed in Supplementary Figure 1 and the dependence of the specific discharge capacities on discharge rate is depicted in Figure 5b. The addition of LFP-350 significantly improves the rate performance of the LFP-50 dominated electrodes with a slight initial capacity reduction. All the electrodes with dominant LFP-350 show superior rate performance compared with both pristine electrodes. In this research, the best rate performance is achieved when LFP-50 and LFP-350 are blended 50:50 with a specific capacity of 81 mAh/g at 10C. The large capacity drop at 15C may be caused by the relatively high loading used in this study and high equivalent series resistance resulting from the coin cell configuration.

Comparison of kinetics for the electrodes

Electrochemical impedance spectroscopy (EIS) is an efficient tool for characterization of electrochemical systems. The evaluations of the impedance spectra, which contain information about the physico-chemical processes inside the cells, are usually conducted by fitting with equivalent

circuit models. In this study, all the EIS spectra are acquired at fully discharged state after the first three cycles at C/10. As displayed in Figure 6a, all the spectra are composed of semicircles within the high-frequency region and Warburg tails followed by sloping lines within the low-frequency region. The impedance data are fitted with the equivalent circuit illustrated in Figure 6c. The intersection with the real axis is the ohmic resistance of the cell (R_1), which is the sum of the contributions from the current collectors, active material, electrolyte and separator[47]. The resistors R_2 and R_3 paralleled with the constant phase element (CPE) account for the contact impedance and charge transfer impedance, respectively[48]. The ion diffusion in the bulk olivine is described with the Warburg element (Z_w) [49]. The resistances obtained from the fittings are summarized in Table 3. It is worth noticing that both the contact resistance and charge transfer resistance of LFP-350 are lower than those of LFP-50, indicating a better packing and a more favorable surface for charge transfer has been obtained with the LFP-350 samples. The mixing of the two LFP particles brings down the contact resistance and the smallest contact resistance is obtained with the mixing ratio of 50:50, suggesting the best packing has been achieved, which is consistent with the results of the density evaluation of the electrodes (summarized in Supplementary Table 1).

The diffusion coefficient of Li ion has been estimated with the following equation,

$$D_{Li} = R^2T^2/2A^2n^4F^4C^2\sigma^2$$

where D_{Li} is the chemical diffusion coefficient for Li ions, R is the gas constant, T is the absolute temperature, A is the electrode area, n is the number of electrons per molecule during oxidation, F is the Faraday constant, C is the concentration of Li ion and σ is the Warburg factor, which can be obtained from the slope of the real impedance vs $\omega^{-1/2}$ (ω is the angular frequency) in the Warburg region. The plots of the real impedance as a function of $\omega^{-1/2}$ and the linear fitting results are illustrated in Figure 6b. The resulting Li diffusion coefficient are summarized in Table 3. The D_{Li} of pristine LFP-350 is higher than that of LFP-50, which may result from the better crystallinity and lower level of anti-site defects (as shown in Table 1) obtained with the higher calcination temperature. Interestingly, by mixing the two pristine LFP particles with the ratio of 50:50, the Li diffusion coefficient has been improved by one order of magnitude. It indicates a modification on the Li diffusion in LFP bulk has been achieved by particle mixing. The increase of Li diffusion coefficient

has been achieved along with the decrease of the contact resistance, indicating the improvement of the packing density facilitates the Li diffusion in the material. Such improvement is not completely surprising since the Li diffusion is an intricate process accompanied by the transport of the electronic carriers to maintain electroneutrality[50].

Mechanism discussion

A better rate capability has been achieved with LFP-350 in this study, although the rate performance is generally expected to be improved with particle size reduction. As mentioned above, the thickness of carbon coating for LFP-50 is expected to be much thinner than that for LFP-350 due to the significantly larger surface area. Therefore, it is likely that a more conductive and homogeneously coated surface has been established on LFP-350 particles, resulting in the charge transfer resistance drop in the EIS and better high rate performance. SEM micrographs of the polished cross-sections of the electrodes made with the two different sizes of pristine LFP and electrodes made with 50:50 mixture are displayed in Supplementary Figure 2 and used to estimate the porosity. Lower porosity has been achieved with the LFP-350 electrode, indicating a better packing compared with LFP-50 electrode. The result is consistent with the density estimation (Supplementary Table 1) and the decrease of the contact resistance can be attributed to the overall improved, electrical connectivity. Furthermore, a lower level of anti-site defects for LFP-350 compared with that of LFP-50 has also been confirmed with the Rietveld refinements of XRD patterns. The anti-site defect has been reported detrimental to the electrochemical performance by blocking the one-dimensional Li diffusion channel[46, 51-54]. Consequently, from all the combined factors just discussed, a better electrochemical performance may have been achieved for LFP-350.

As shown in Supplementary Figure 2, the two kinds of particles are uniformly distributed, and the porosity is decreased in the mixed electrode, which suggests that a better contact among the particles has been achieved, without limiting the access to the electrolyte. The two as-prepared LFP particles exhibit different phase transitions during charging and discharging, especially at high C-rates. Schematic illustrations are shown in Figure 7. The sloping voltage profile of LFP particles with ~50 nm has been reported resulting from single-phase Li-insertion previously[13] (as shown in Figure 7a), which is expected to be favorable for rapid charge and discharge. However, the loss of the voltage

plateau sacrifices the energy density. Comparing with small LFP particles, two-phase Li insertion is observed in larger LFP particles (~350 nm in this study). The phase transition starts with a noticeable voltage overshoot in the charge-discharge profile (Figure 7b). The voltage overshoot has been reported as necessary to facilitate the successive phase transition of large crystallites, as there is less specific surface and fewer defects acting as nucleation sites[55]. With the growth of the new phase inside the particle, the cell voltage remains almost independent with the intercalation of Li within the two-phase region.

Therefore, by mixing the particles with different phase transition mechanisms, we can take the best of both sides. As the single-phase Li insertion/extraction is faster than the two-phase Li insertion/extraction, the particles with single-phase Li insertion can be the reservoir of Li ion. Taking the charge process for explanation, as shown in Figure 7c, the Li extraction at the beginning of charge would happen in the small particles with single-phase insertion mechanism, which eliminates the initial voltage overshoot. During the following charge, charge transfer between the large and small particles would occur and the two-phase Li extraction starts providing the flat voltage plateau. In the meantime, the small particles which lost the Li ions to the large particles can continuously get Li ions from the electrolyte. As a consequence, the presence of the single-phase insertion particles in the electrode can reduce the polarization caused by fast charge/discharge and deliver improved rate performance.

Conclusions

In summary, the rate performance of the LFP electrode has been improved by blending LFP particles of two different particle sizes and Li insertion mechanisms. The optimization of the particle size distribution offers better packing density and contact of the active material particles. The improvement of packing results in better pathway for electron transport and lower contact resistance. In the meantime, LFP particles with single-phase Li insertion mechanism reduce the polarization of the cell at high C-rate by acting as the reservoir of Li ions. In this study, the electrode with a mixing ratio of 50:50 shows an improved initial capacity at C/10 and superior rate capability compared with the two pristine materials.

Acknowledgement

Yin Zhang would like to acknowledge CSIRO for the studentship, and the involvement of CRRC and the Rail Manufacturing Cooperative Research Centre (funded jointly by participating rail organisations and the Australian Federal Government's Cooperative Research Centres Program). The experimental data reported in this paper were obtained at the Central Analytical Research Facility operated by the Institute for Future Environments, Queensland University of Technology (QUT), Brisbane, Australia. The synchrotron based sXAS data reported in this paper were obtained at the soft X-ray beamline of Australian Synchrotron (AS). The authors would like to acknowledge Mr. Mark Quinlan and Felix Lo, QUT, for the assistance with sample synthesis. The authors would like to acknowledge Dr. Michael Jones, QUT, for the assistance with the application for soft x-ray beamline at AS.

References

1. J. D. Wilcox, M. M. Doeff, M. Marcinek, and R. Kostecki, *J. Electrochem. Soc.*, **154** (5), A389-A395 (2007).
2. L. Chen, Y.-Q. Yuan, X. Feng, and M.-W. Li, *J. Power Sources*, **214** 344-350 (2012).
3. X.-C. Tang, L.-X. Li, Q.-L. Lai, X.-W. Song, and L.-H. Jiang, *Electrochim. Acta*, **54** (8), 2329-2334 (2009).
4. S. Deng, H. Wang, H. Liu, J. Liu, and H. Yan, *Nano-Micro Letters*, **6** (3), (2014).
5. A. Yamada and S.-C. Chung, *J. Electrochem. Soc.*, **148** (8), A960 (2001).
6. W.-J. Zhang, *J. Power Sources*, **196** (6), 2962-2970 (2011).
7. S. Y. Chung, J. T. Bloking, and Y. M. Chiang, *Nat. Mater.*, **1** (2), 123-128 (2002).
8. E. M. Bauer, C. Bellitto, M. Pasquali, P. P. Prosini, and G. Righini, *Electrochem. Solid-State Lett.*, **7** (4), A85-A87 (2004).
9. D.-H. Kim and J. Kim, *Electrochem. Solid-State Lett.*, **9** (9), A439-A442 (2006).
10. D. Morgan, A. Van der Ven, and G. Ceder, *Electrochem. Solid-State Lett.*, **7** (2), A30-A32 (2004).
11. S.-i. Nishimura, G. Kobayashi, K. Ohoyama, R. Kanno, M. Yashima, and A. Yamada, *Nat. Mater.*, **7** (9), 707-711 (2008).
12. R. Malik, D. Burch, M. Bazant, and G. Ceder, *Nano Lett.*, **10** (10), 4123-4127 (2010).
13. P. Gibot, M. Casas-Cabanas, L. Laffont, S. Levasseur, P. Carlach, S. Hamelet, J. M. Tarascon, and C. Masquelier, *Nat. Mater.*, **7** (9), 741-747 (2008).
14. G. Kobayashi, S.-i. Nishimura, M.-S. Park, R. Kanno, M. Yashima, T. Ida, and A. Yamada, *Adv. Funct. Mater.*, **19** (3), 395-403 (2009).
15. Z. Li, J. Yang, C. Li, S. Wang, L. Zhang, K. Zhu, and X. Wang, *Chem. Mater.*, **30** (3), 874-878 (2018).
16. N. Meethong, H.-Y. S. Huang, W. C. Carter, and Y.-M. Chiang, *Electrochem. Solid-State Lett.*, **10** (5), A134-A138 (2007).
17. Y.-S. Yu, C. Kim, D. A. Shapiro, M. Farmand, D. Qian, T. Tyliszczak, A. D. Kilcoyne, R. Celestre, S. Marchesini, and J. Joseph, *Nano Lett.*, **15** (7), 4282-4288 (2015).
18. W. Dreyer, J. Jamnik, C. Guhlke, R. Huth, J. Moškon, and M. Gaberšček, *Nat. Mater.*, **9** (5), 448 (2010).
19. W. C. Chueh, F. El Gabaly, J. D. Sugar, N. C. Bartelt, A. H. McDaniel, K. R. Fenton, K. R. Zavadil, T. Tyliszczak, W. Lai, and K. F. McCarty, *Nano Lett.*, **13** (3), 866-872 (2013).

20. D. Li, X. Liu, and H. Zhou, *Energy Technol.*, **2** (6), 542-547 (2014).
21. T. Zhang, X. Liu, P. He, R. Peng, M. Wang, M. Han, and H. Zhou, *J. Power Sources*, **233** 299-303 (2013).
22. X. Guo, B. Song, G. Yu, X. Wu, X. Feng, Li, and Y. Chen, *ACS Appl. Mater. Interfaces*, (2018).
23. C. M. Doherty, R. A. Caruso, and C. J. Drummond, *Energy Environ. Sci.*, **3** (6), (2010).
24. J. Wu, G. K. P. Dathar, C. Sun, M. G. Theivanayagam, D. Applestone, A. G. Dylla, A. Manthiram, G. Henkelman, J. B. Goodenough, and K. J. Stevenson, *Nanotechnology*, **24** (42), 424009 (2013).
25. Y. Liu, J. Liu, J. Wang, M. N. Banis, B. Xiao, A. Lushington, W. Xiao, R. Li, T. K. Sham, G. Liang, and X. Sun, *Nature Communications*, **9** (1), 929 (2018).
26. Y.-H. Rho, L. F. Nazar, L. Perry, and D. Ryan, *J. Electrochem. Soc.*, **154** (4), A283-A289 (2007).
27. S. Uchida, M. Yamagata, and M. Ishikawa, *J. Power Sources*, **243** 481-487 (2013).
28. E. Ershenko, A. Bobyl, M. Boiko, Y. Zubavichus, V. Runov, M. Trenikhin, and M. Sharkov, *Ionics*, **23** (9), 2293-2300 (2017).
29. Y. Zhang, J. A. Alarco, A. S. Best, G. A. Snook, P. C. Talbot, and J. Y. Nerkar, *RSC Adv.*, **9** (2), 1134-1146 (2019).
30. W.-J. Zhang, *J. Electrochem. Soc.*, **157** (10), A1040-A1046 (2010).
31. J. J. Biendicho and A. R. West, *Solid State Ionics*, **203** (1), 33-36 (2011).
32. S. L. Bewlay, K. Konstantinov, G. X. Wang, S. X. Dou, and H. K. Liu, *Mater. Lett.*, **58** (11), 1788-1791 (2004).
33. K. Hoang and M. Johannes, *Chem. Mater.*, **23** (11), 3003-3013 (2011).
34. S. Yang, D. Wang, G. Liang, Y. M. Yiu, J. Wang, L. Liu, X. Sun, and T.-K. Sham, *Energy Environ. Sci.*, **5** (5), 7007 (2012).
35. X. Liu, D. Wang, G. Liu, V. Srinivasan, Z. Liu, Z. Hussain, and W. Yang, *Nature Communications*, **4** 2568 (2013).
36. T. K. Sham, *Adv. Mater.*, **26** (46), 7896-7901 (2014).
37. R. Brydson, B. Williams, W. Engel, H. Sauer, E. Zeitler, and J. Thomas, *SSCom*, **64** (4), 609-612 (1987).
38. A. Augustsson, G. V. Zhuang, S. M. Butorin, J. M. Osorio-Guillen, C. L. Dong, R. Ahuja, C. L. Chang, P. N. Ross, J. Nordgren, and J. H. Guo, *The Journal of Chemical Physics*, **123** (18), 184717 (2005).
39. P. Sarode, *Journal of Physics F: Metal Physics*, **17** (7), 1605 (1987).

40. F. De Groot, M. Grioni, J. C. Fuggle, J. Ghijsen, G. A. Sawatzky, and H. Petersen, *PhRvB,* **40** (8), 5715 (1989).
41. J. McBreen, *Journal of Solid State Electrochemistry,* **13** (7), 1051-1061 (2009).
42. J. G. Lapping, S. A. Delp, J. L. Allen, J. L. Allen, J. W. Freeland, M. D. Johannes, L. Hu, D. T. Tran, T. R. Jow, and J. Cabana, *Chem. Mater.,* **30** (6), 1898-1906 (2018).
43. K. Nakanishi and T. Ohta, *Surf Interface Anal,* **44** (6), 784-788 (2012).
44. A. S. Andersson, B. Kalska, L. Häggström, and J. O. Thomas, *Solid State Ionics,* **130** (1), 41-52 (2000).
45. K. Zaghib, A. Mauger, F. Gendron, and C. M. Julien, *Chem. Mater.,* **20** (2), 462-469 (2008).
46. P. Axmann, C. Stinner, M. Wohlfahrt-Mehrens, A. Mauger, F. Gendron, and C. Julien, *Chem. Mater.,* **21** (8), 1636-1644 (2009).
47. D. Andre, M. Meiler, K. Steiner, C. Wimmer, T. Soczka-Guth, and D. U. Sauer, *J. Power Sources,* **196** (12), 5334-5341 (2011).
48. Y. Zhu, Y. Xu, Y. Liu, C. Luo, and C. Wang, *Nanoscale,* **5** (2), 780-787 (2013).
49. J. Gerschler and D. Sauer. Bruxelles, 2007.
50. N. Vicente, M. Haro, and G. J. C. c. Garcia-Belmonte, **54** (9), 1025-1040 (2018).
51. J. Chen and J. Graetz, **3** (5), 1380-1384 (2011).
52. S.-Y. Chung, S.-Y. Choi, S. Lee, and Y. J. P. r. l. Ikuhara, **108** (19), 195501 (2012).
53. Q. D. Truong, M. K. Devaraju, T. Tomai, I. J. A. a. m. Honma, and interfaces, **5** (20), 9926-9932 (2013).
54. J. Jacas Biendicho, K.-C. Hsiao, S. Hull, and A. R. J. I. c. West, **56** (6), 3657-3662 (2017).
55. J. Jia, C. Tan, M. Liu, D. Li, and Y. Chen, *ACS Appl. Mater. Interfaces,* **9** (29), 24561-24567 (2017).

401 # Tables

402 *Table 1 Rietveld refinement results for the as-prepared LFP samples.*

Sinter temperature	710 °C	550 °C
a/Å	10.3257	10.3190
b/Å	6.0062	6.0021
c/Å	4.6917	4.6919
α/°	90	90
β/°	90	90
γ/°	90	90
Cell volume/ $Å^3$	290.97	290.597
Fe_{Li}/%	0.84	1.98
R_{wp}/%	3.30	2.23
R_{Bragg}/%	1.86	1.54

403

404 *Table 2 Mole ratios of lithium, iron and phosphorus obtained by ICP and carbon content for the LFP samples.*

Sample	Li:Fe:P	Carbon content/ wt.%
LFP-350	1.06(5):1:0.97(3)	1.91±0.07
LFP-50	1.05(4):1:0.98(0)	2.77±0.03

405

406 *Table 3 Fitting results of the high-resolution XPS spectra for the LFP samples.*

Sample	Fe^{2+} 2p			Fe^{3+} 2p		
	$2p_{3/2}$	$2p_{1/2}$	%	$2p_{3/2}$	$2p_{1/2}$	%
LFP-350	710.8	724.2	49.8	713.2	726.9	50.2
LFP-50	710.7	724.0	48.8	713.2	726.8	51.2

Table 4 Resistances and Li diffusion coefficients obtained from EIS results.

	LFP-50	80:20	60:40	50:50	40:60	20:80	LFP-350
R_1/Ω	4.81	3.38	6.17	4.34	3.24	7.02	5.84
R_2/Ω	3.67	1.26	1.32	0.67	1.29	3.21	2.86
R_3/Ω	8.18	7.91	6.87	5.24	6.69	4.23	2.08
$D_{Li}/\times10^{-14}$ cm^2/s	1.25	2.27	2.22	10.62	2.29	1.99	3.16

Figures

Figure 1 XRD and Rietveld refinement for the as-prepared LFP samples sintered at (a) 710 and (b) 550 ℃, respectively.

Figure 2 SEM, TEM micrographs and high-resolution XPS spectra for (a-c) LFP-350 and (d-f) LFP-50.

Figure 3 NEXAFS for the LFP samples. (a) Fe L-edge and O K-edge for (b) LFP-350 and (c) LFP-50. The green, pink and blue lines in (b) and (c) are the O K-edge collected with PEY, TEY and TFY mode, respectively.

Figure 4 Galvanostatic charge and discharge of the pristine materials (a-b) LFP-350 and (c-d) LFP-50. (b) and (d) is the partial enlarged voltage plateau of (a) and (c), respectively.

Figure 5 (a) Galvanostatic charge-discharge profiles of the pristine and mixed electrodes at C/10. (b) Comparison of rate capabilities of the pristine and mixed electrodes.

Figure 6 (a) EIS spectra, (b) plots of the real impedance as a function of the square root of angular frequency at low-frequency region and (c) the equivalent circuit of the LFP electrodes.

Figure 7 Schematic of the LFP electrodes during charging. (a) LFP-50, (b) LFP-350 and (c) mixed electrodes.

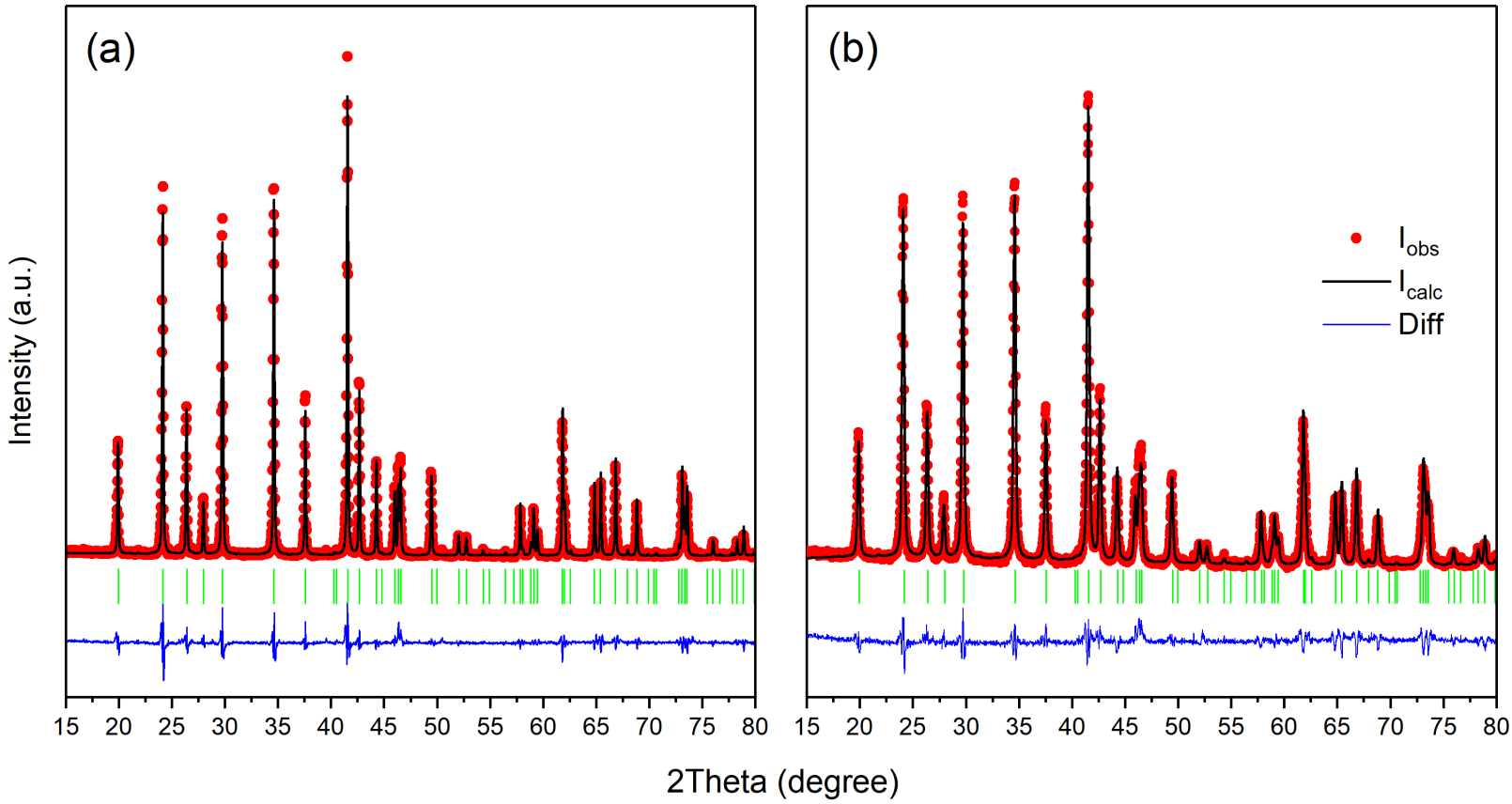
(a)
(b)
Intensity (a.u.)
2Theta (degree)
I_obs
I_calc
Diff
15 20 25 30 35 40 45 50 55 60 65 70 75 80

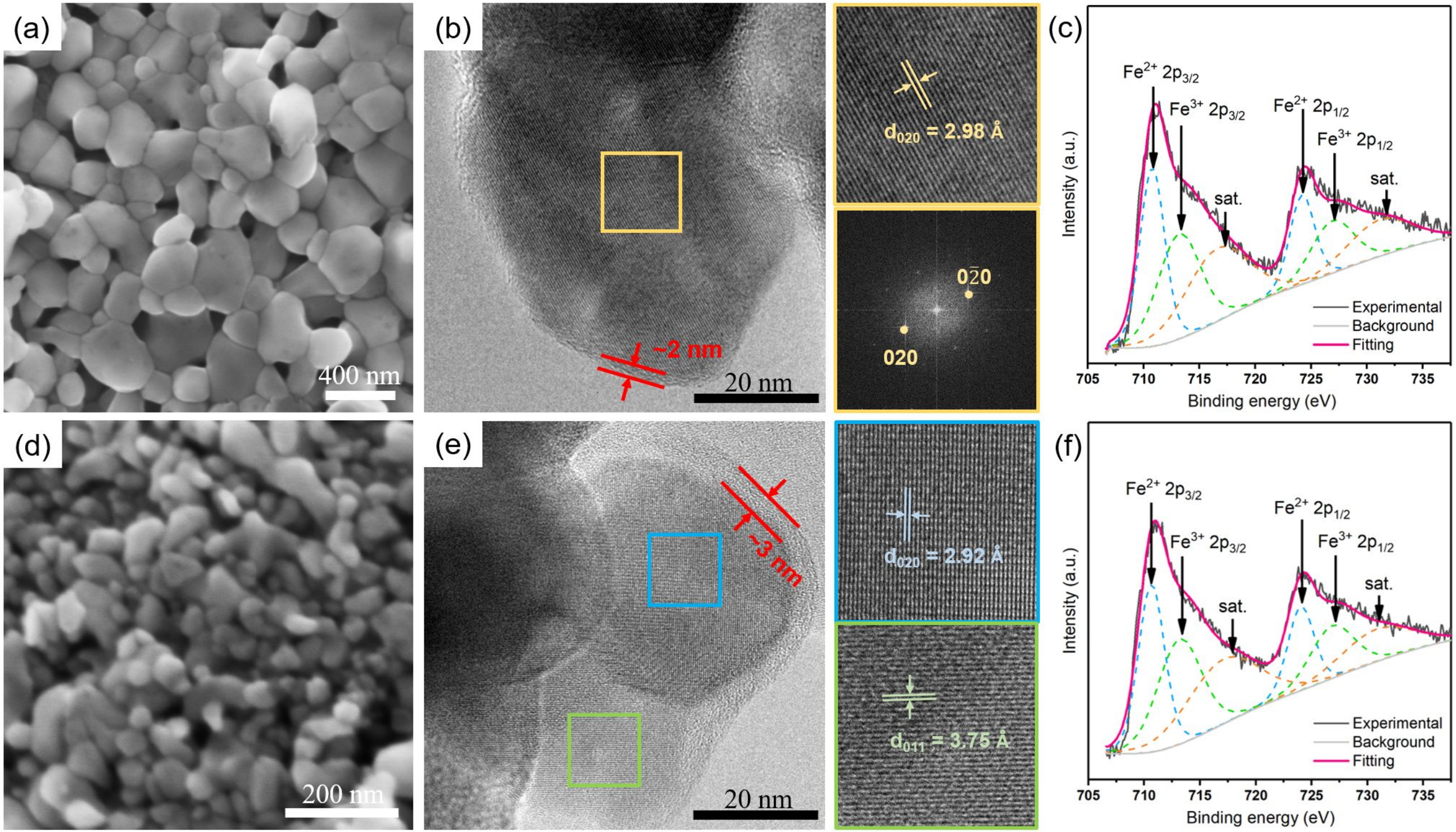
(a)
400 nm
(b)
~2 nm
20 nm
d_{020} = 2.98 Å
$0\bar{2}0$
020
(c)
Fe^{2+} $2p_{3/2}$
Fe^{3+} $2p_{3/2}$
sat.
Fe^{2+} $2p_{1/2}$
Fe^{3+} $2p_{1/2}$
sat.
Intensity (a.u.)
Experimental
Background
Fitting
705 710 715 720 725 730 735
Binding energy (eV)
(d)
200 nm
(e)
~3 nm
20 nm
d_{020} = 2.92 Å
d_{011} = 3.75 Å
(f)
Fe^{2+} $2p_{3/2}$
Fe^{3+} $2p_{3/2}$
sat.
Fe^{2+} $2p_{1/2}$
Fe^{3+} $2p_{1/2}$
sat.
Intensity (a.u.)
Experimental
Background
Fitting
705 710 715 720 725 730 735
Binding energy (eV)

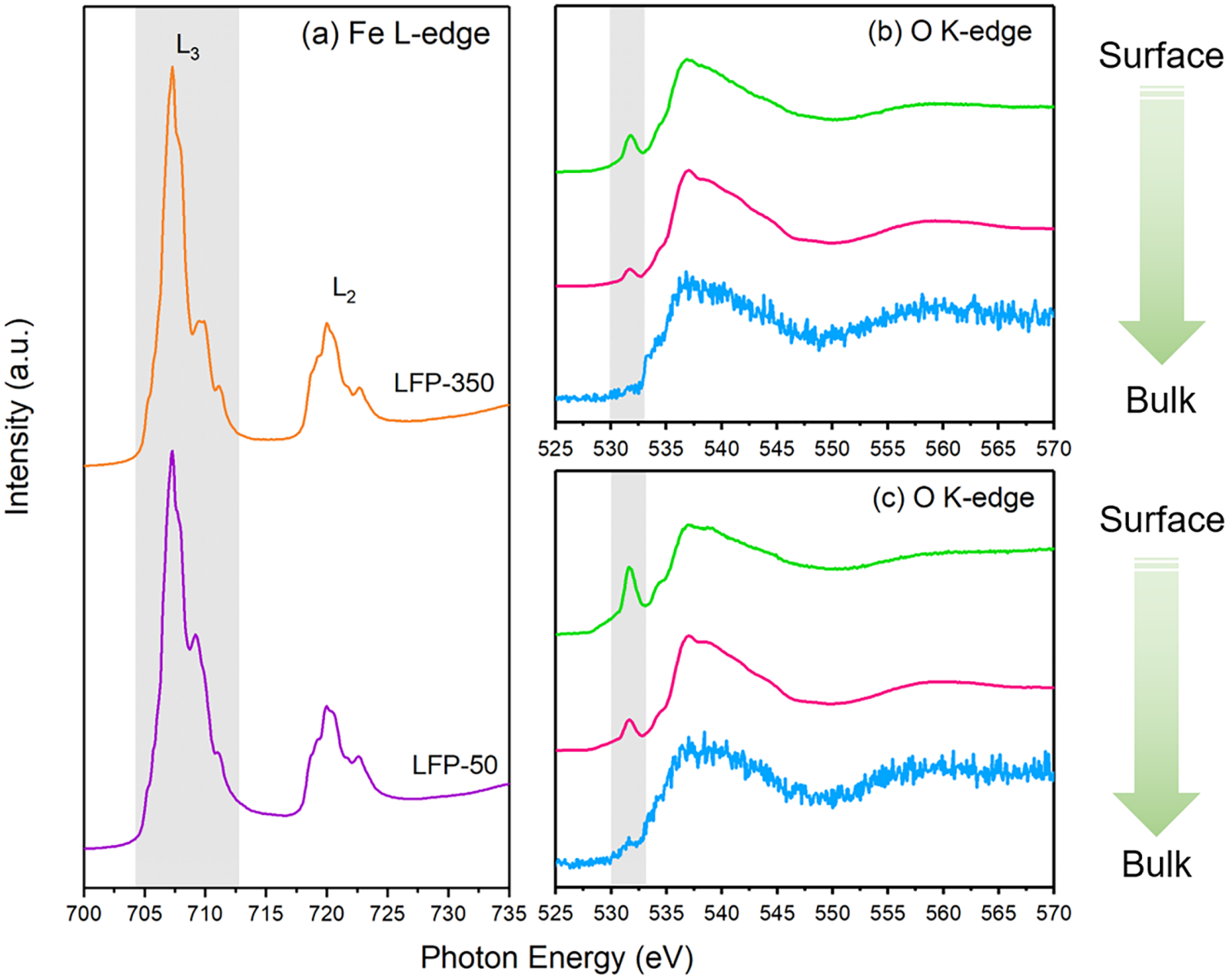
(a) Fe L-edge
L3
L2
LFP-350
LFP-50
Intensity (a.u.)
700 705 710 715 720 725 730 735
Photon Energy (eV)
(b) O K-edge
525 530 535 540 545 550 555 560 565 570
Surface
Bulk
(c) O K-edge
525 530 535 540 545 550 555 560 565 570
Surface
Bulk

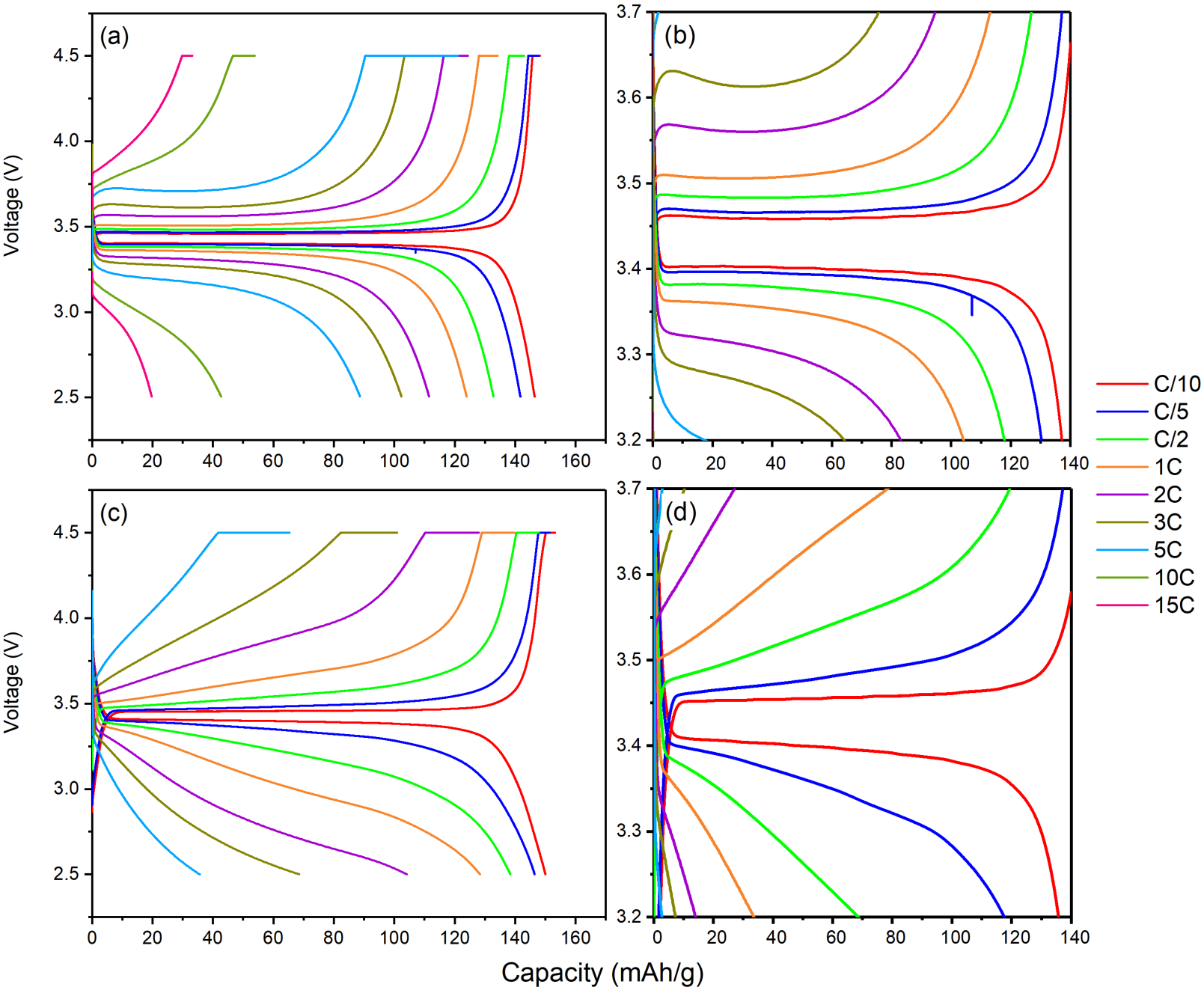
(a)
(b)
(c)
(d)
Voltage (V)
Capacity (mAh/g)
C/10
C/5
C/2
1C
2C
3C
5C
10C
15C

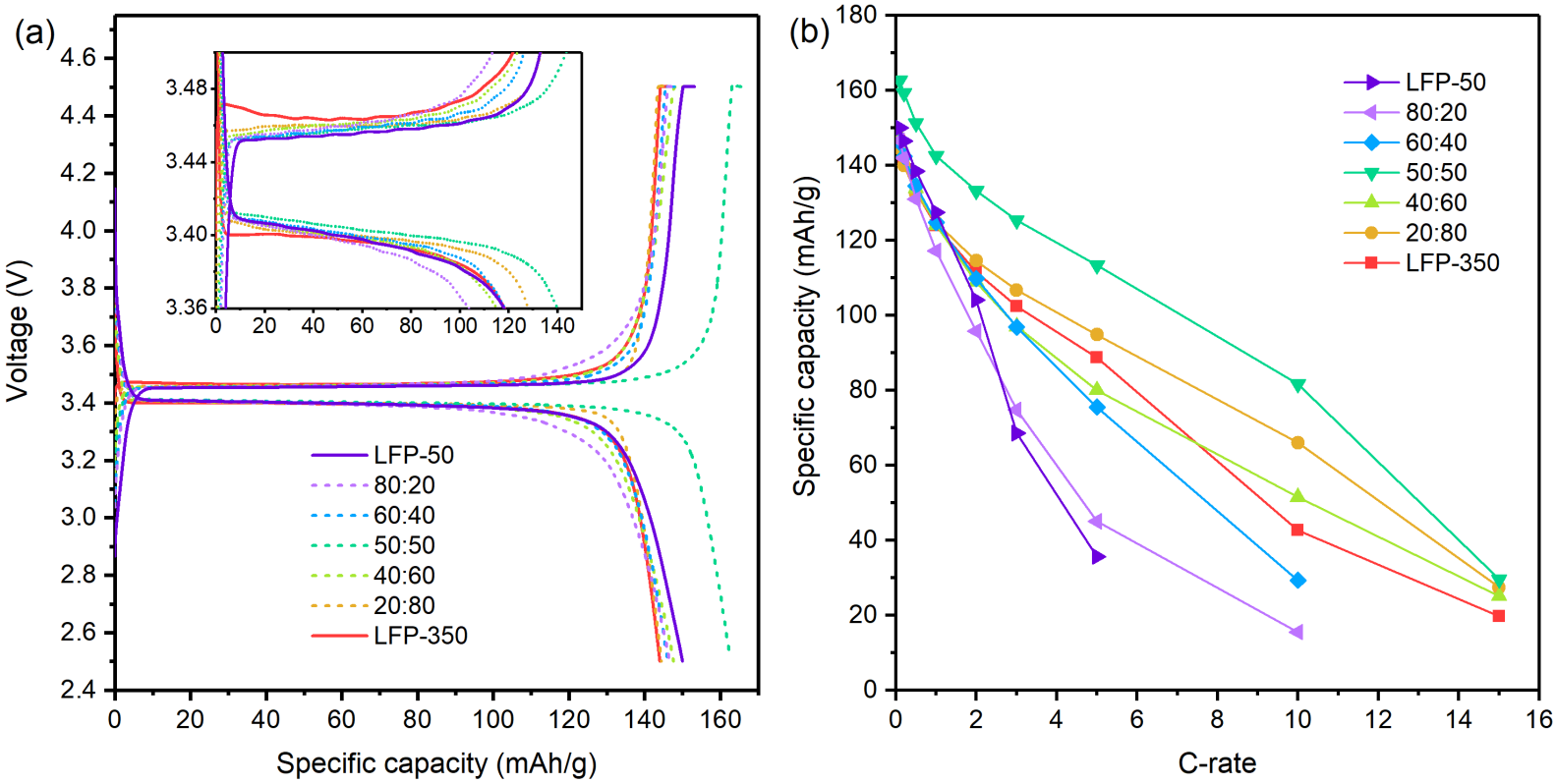
(a)
Voltage (V)
Specific capacity (mAh/g)
LFP-50
80:20
60:40
50:50
40:60
20:80
LFP-350
(b)
Specific capacity (mAh/g)
C-rate
LFP-50
80:20
60:40
50:50
40:60
20:80
LFP-350

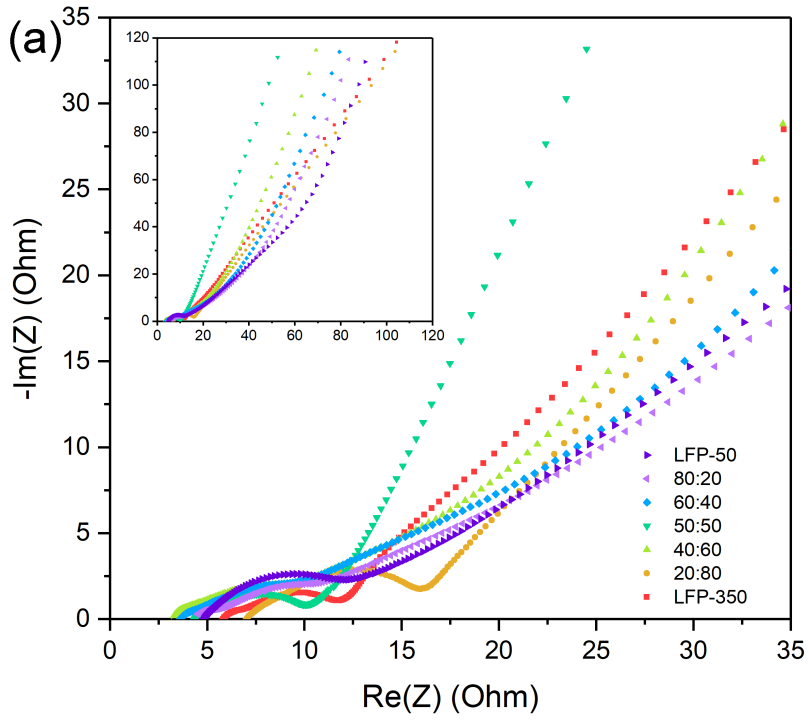
(a)
-Im(Z) (Ohm)
Re(Z) (Ohm)
LFP-50
80:20
60:40
50:50
40:60
20:80
LFP-350

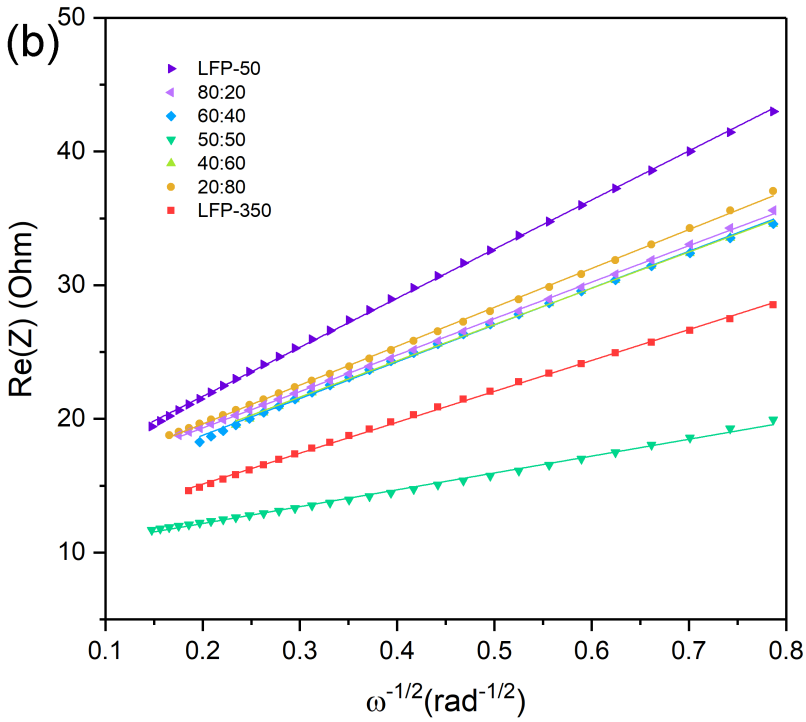
(b)
Re(Z) (Ohm)
ω-1/2(rad-1/2)
LFP-50
80:20
60:40
50:50
40:60
20:80
LFP-350

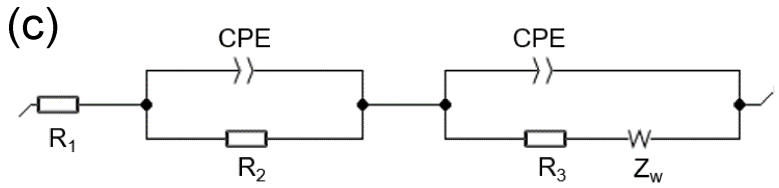
(c)
CPE
CPE
R1
R2
R3
W
Zw

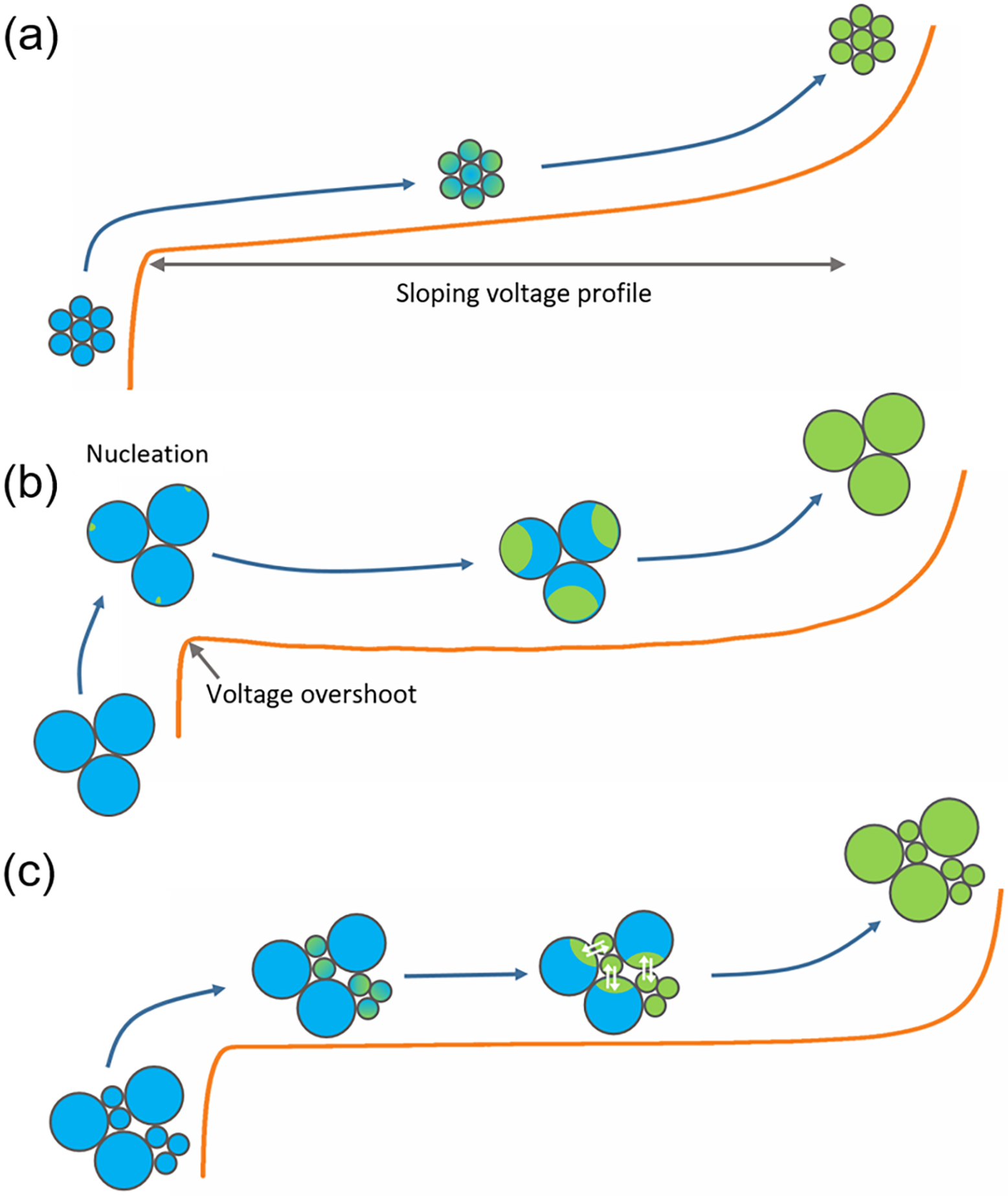
(a)
Sloping voltage profile
(b)
Nucleation
Voltage overshoot
(c)